Journal of
Materials Chemistry B

ROYAL SOCIETY
OF CHEMISTRY

PAPER

View Article Online
View Journal | View Issue

Check for updates

Cite this: *J. Mater. Chem. B*, 2024, **12**, 3404

Enzyme-triggered on-demand release of a H_2O_2-self-supplying $CuO_2@Fe_3O_4$ nanoagent for enhanced chemodyamic antimicrobial therapy and wound healing†

Sijie Zhang,[ab] Sameer Hussain,[a] Yuhai Tang,[a] Kaili Wang,[b] Xingyan Wang,[a] Long Zhang,[b] Yuheng Liao,[c] Chen Wang,[c] Yi Hao*[ab] and Ruixia Gao*[a]

Received 20th November 2023,
Accepted 7th March 2024

DOI: 10.1039/d3tb02762g

rsc.li/materials-b

Nanoagents for chemodynamic therapy (CDT) hold a promising future in the field of antimicrobials, especially copper peroxide (CuO_2) (CP) nanomaterials which have garnered significant attention due to their ability to self-supply H_2O_2. Nevertheless, the poor stability of CuO_2 remains a critical challenge which restricts its practical application in the antibacterial field. In this study, an advanced nano-antimicrobial system HA-CP@Fe_3O_4 with enzyme-responsive properties is developed by coating hyaluronic acid (HA) on CuO_2-loaded iron tetraoxide nanoparticles. The coating of HA not only stabilizes the CuO_2 nanomaterials but also provides responsiveness towards the enzyme hyaluronidase, which is typically secreted by some bacteria. The outer layer of HA in HA-CP@Fe_3O_4 undergoes decomposition in the presence of hyaluronidase-secreting bacteria, resulting in the release of $CuO_2@Fe_3O_4$. The released $CuO_2@Fe_3O_4$ then self-supplies H_2O_2 and generates reactive oxygen species (ROS) within the infected microenvironment through Fenton and Russell effects, to ultimately achieve effective and precise antimicrobial activity. Simultaneously, the magnetic property provided by Fe_3O_4 allows the substance to be directed towards the infection site. Both *in vitro* and *in vivo* tests demonstrated that HA-CP@Fe_3O_4 exhibited excellent antimicrobial capabilities at low concentration (30 μg mL^{-1}), exceptional biocompatibility and the ability to accelerate wound healing. The findings of this work offer a new and promising approach for targeted and precise CDT.

1. Introduction

Global health has long been seriously threatened by bacterial diseases.[1–3] Antibiotics have been the mainstay of conventional treatments, but their overuse and widespread misuse have led to the expression of drug-resistant genes in bacteria,[4–7] making it increasingly challenging to treat bacterial infections.[8,9] Significant efforts have been made to develop novel bactericidal strategies that do not rely on antibiotics, aiming to circumvent the drawbacks of conventional antibiotic therapy.[10–14] Specifically, chemodynamic therapy (CDT), which is based on the Fenton or Fenton-like reaction, stimulates the generation of highly toxic hydroxyl radicals ($^{\bullet}OH$) from hydrogen peroxide (H_2O_2) to achieve antibacterial activity.[15–17] CDT is a very promising antibacterial technique owing to low treatment costs and independence from environmental cues.[18–20] However, the antibacterial efficacy of conventional CDT nanomaterials against bacterial infections has been restricted by the low concentrations of H_2O_2 in the targeted area.[21,22] Exogenous H_2O_2 is often required for effective sterilization to resolve this issue, but it can cause damage to healthy tissues during wound healing. Therefore, it is crucial to develop advanced nano-antimicrobial CDT systems that can provide enhanced antimicrobial activity without the need of exogenous H_2O_2.

Copper peroxide (CuO_2) is an emerging bactericidal material composed of copper ions and peroxy groups. It has the ability to self-supply H_2O_2 and convert it into highly reactive hydroxyl radicals ($^{\bullet}OH$) for realizing augmented antibacterial treatment.[23,24] Typically, CuO_2 undergo decomposition in an infected microenvironment, resulting in the formation of Cu^{2+} and H_2O_2. Subsequently, a Fenton reaction occurs between Cu^{2+} and H_2O_2, leading to the generation of $^{\bullet}OH$, which effectively kills bacteria. Despite being an ideal antibacterial material, the practical use of CuO_2 in CDT has been hindered due to its inherent instability. Recently, significant

---

[a] School of Chemistry, Xi'an Jiaotong University, Xi'an, Shaanxi 710049, China. E-mail: haoyi8904@xjtu.edu.cn, ruixiagao@xjtu.edu.cn
[b] School of Pharmacy, Xi'an Jiaotong University, Xi'an, Shaanxi 710061, China
[c] Health Science Center, Xi'an Jiaotong University, Xi'an, Shaanxi 710061, China

† Electronic supplementary information (ESI) available. See DOI: https://doi.org/10.1039/d3tb02762g

efforts have been made to improve the stability of CuO_2 by using carriers such as molybdenum disulfide (MoS_2) nanospheres, titanium oxide (TiO_2) nanosheets, and polydopamine (PDA) nanoparticles.[25–27] However, these nanocomposites lack ability to effectively accumulate at the targeted site and inevitably cause damage to normal tissues. Therefore, it is crucial to select appropriate carriers that not only enhance the stability and utilization of CuO_2 but also minimize harm to healthy tissues.

Meanwhile, iron tetraoxide (Fe_3O_4) has been widely used in antimicrobial applications due to its excellent biocompatibility.[28,29] Iron ions derived from Fe_3O_4 can generate reactive oxygen species (ROS) through the Fenton effect, thereby exhibiting strong antibacterial properties.[30–32] In addition, the magnetic properties of Fe_3O_4 have attracted significant attention from researchers. Fe_3O_4 can be effectively combined with other materials to impart magnetic properties to nanomaterials for realizing targeted therapy and/or recycling process.[33–37] For instance, Liu and colleagues prepared a smart drug delivery system based on iron oxide nanoparticles by utilizing a focal pyroptosis-starvation-chemotherapy strategy.[38] Liu *et al.* designed UCNP/Fe_3O_4 nanoparticles for photodynamic therapy of cancer.[39] Feng *et al.* developed magnetic manganese oxide sweetgum-ball nanospheres for chemotherapy and photodynamic therapy of cancer.[40] All of these studies have utilized the magnetic properties of Fe_3O_4 to facilitate the aggregation of nanomaterials/drugs at the tumor site, resulting in efficient utilization of materials and enhanced therapeutic efficacy. However, to the best of our knowledge, magnetic aggregation therapy has been rarely studied in the field of antimicrobial research. Therefore, based on the Fenton effect and the magnetic aggregation property of Fe_3O_4, we hypothesize that the modification of magnetic nanomaterials can further enhance the utilization rate of CuO_2 and facilitate the dual Fenton effect. Besides, hyaluronic acid (HA) has also been extensively used in medicine due to its excellent biocompatibility. Interestingly, HA can only be degraded by the action of enzyme hyaluronidase (HAase) secreted by some bacteria.[41–43] Consequently, by coating magnetic nanomaterials exhibiting dual Fenton effect with HA, it is possible to achieve precise control over the release of nanomaterials and further improve the bactericidal rate.

In this study, we successfully developed a robust nanocomposite system, HA-CP@Fe_3O_4, with enzyme-responsive properties for enhanced chemodyamic antimicrobial therapy involving self-supplied H_2O_2 (Scheme 1). To prepare HA-CP@Fe_3O_4, carboxylated iron tetraoxide (Fe_3O_4–COOH) was utilized as a carrier to improve the stability of CuO_2. This was achieved by leveraging the reaction between carboxyl groups and copper ions to facilitate the *in situ* growth of CuO_2 on the surface of the carrier. Subsequently, the resulting material was coated with HA to prevent the decomposition of CuO_2 and the release of copper ions, resulting in the desired biocompatible nanocomposite, HA-CP@Fe_3O_4. Interestingly, HA-CP@Fe_3O_4 can be aggregated at the infection site under the influence of an applied magnetic field and release CuO_2@Fe_3O_4 through destruction of outer HA layer in the presence of target HAase secreting bacteria. In the acidic environment of the infection site, CuO_2@Fe_3O_4 then decomposes into Cu^{2+}, iron ions and H_2O_2. CuO_2 and iron ions can induce CDT by converting H_2O_2 to $^{\bullet}OH$ through the Fenton effect. Simultaneously, Cu^{2+} catalyzes the production of singlet oxygen ($^1O_2$) for CDT through

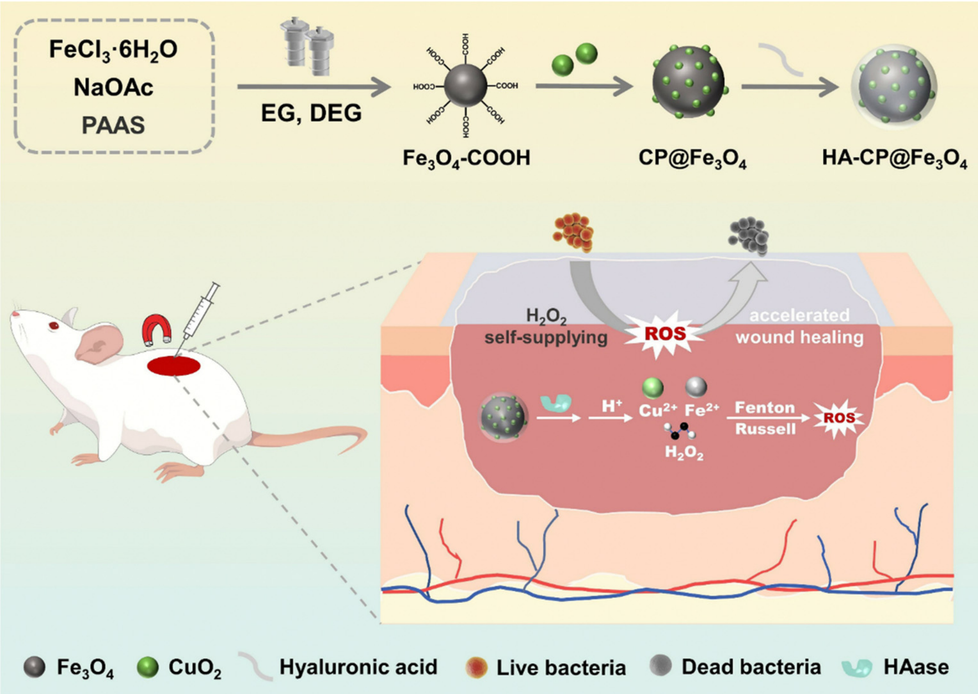

Scheme 1 Schematic diagram of the preparation of the enzyme-responsive nanoplatform HA-CP@Fe_3O_4 and its application in the study of antibacterial infection *in vivo*.

the Russell effect. Therefore, HA-CP@Fe_3O_4 can be precisely released at the site of infection using the magnetic properties of Fe_3O_4 and the enzyme responsiveness conferred by HA, to ultimately reduce the antimicrobial dose and boost the overall antimicrobial activity of CDT. The outstanding antimicrobial activity of HA-CP@Fe_3O_4 *via* CDT was validated through both vitro and *in vivo* studies. This work presents an attractive strategy for developing a powerful antibacterial platform using controlled release in CDT.

2. Experimental section

2.1 Materials

Copper chloride ($CuCl_2{\cdot}2H_2O$), 3,3′,5,5′-tetramethylbenzidine (TMB), methylene blue (MB), 1,3-diphenylisobenzofuran (DPBF), glutathione (GSH), isopropyl alcohol (IPA), 1,4-benzoquinone (BQ) and L-histidine (His) were provided by Aladdin Chemical Reagent Co., Ltd (China). Poly(vinylpyrrolidone) (PVP), potassium iodide (KI), sodium polyacrylate (PAAS), sodium hyaluronate (HA) and hyaluronidase (HAase) were obtained from Shanghai Macklin Biochemical Technology Co., Ltd (China). Ferric chloride hexahydrate ($FeCl_3{\cdot}6H_2O$), anhydrous sodium acetate (NaOAc), diethylene glycol (DEG), ethylene glycol (EG), glutaraldehyde (GA) were provided by Tianjin Kermel chemical reagent factory (China). Hydrogen peroxide (H_2O_2, 30%), potassium permanganate ($KMnO_4$) 5,5′-dithiobis (2-nitrobenzoic acid) (DTNB) and sodium hydroxide (NaOH) were obtained from Sinopharm Chemical Reagent Co., Ltd. Sodium acetate buffer solution (NaAc buffer) and phosphate buffer solution (PBS) were provided by Shaanxi Zhonghuihecai Biomedical Technology Co., Ltd (China). LB broth and plate counting agar were purchased from Beijing Aoboxing Biotechnology Co., Ltd (China). All analytical reagents are used immediately without any purification. Ultrapure water was used in all experiments.

2.2 Synthesis of HA-CP@Fe_3O_4

Synthesis of Fe_3O_4–COOH: Fe_3O_4–COOH was synthesized by a straightforward one-pot hydrothermal process. In brief, $FeCl_3{\cdot}6H_2O$ (0.504 g), NaOAC (2 g), and PAAS (50 mg) were added to a mixture of $C_2H_5OH/C_4H_{10}O_3$ (7/13 mL) and subjected to ultrasonication. Then, the reaction mixture was heated at 200 °C for 12 h. After the completion of reaction, the reaction mixture was allowed to cool followed by washing with ultrapure water and finally dried at 40 °C to obtain Fe_3O_4–COOH.

Synthesis of CuO_2@Fe_3O_4 (CP@Fe_3O_4): $CuCl_2{\cdot}2H_2O$ (50 mL, 0.01 M) was added to a reaction flask containing Fe_3O_4–COOH (50 mg) and the mixture was mechanically stirred for 4 h. Afterwards, PVP (3 g), NaOH (50 mL, 0.02 M), and H_2O_2 (1 mL, 10 M) were added sequentially. The reaction mixture was stirred continuously for 30 min followed by washing with ultra-pure water. The product was freeze-dried to finally obtain CP@Fe_3O_4.

Synthesis of HA-CuO_2@Fe_3O_4 (HA-CP@Fe_3O_4): firstly, CuO_2@Fe_3O_4 (50 mg) was dispersed in aqueous $CuCl_2{\cdot}2H_2O$ (50 mL, 0.01 M), and stirred for 4 h. Then, HA (50 mL, 0.5 mg mL^{-1}) was introduced, and the reaction mixture was stirred continuously for another 12 h. After washing the product with ultra-pure water and subjected to freeze-drying, HA-CP@Fe_3O_4 was finally obtained. The atomic absorption spectrometer (AAS, AA-6880, Shimadzu Co., Japan) was used to further measure the amount of CuO_2 in HA-CP@Fe_3O_4.

2.3 Monitoring the release of copper ion and H_2O_2 from HA-CP@Fe_3O_4

Release of copper ion: HA-CP@Fe_3O_4 was dispersed in PBS (pH = 7.4) or NaAc buffer (pH = 5.4) in the absence and presence of HAase (150 U mL^{-1}), respectively. The mixture was continuously stirred at 37 °C to simulate the physiological environment. The dialysate was collected after the appropriate time, and buffer solution was replenished. Atomic absorption spectrometer was used to detect the release of copper ions.

Release of H_2O_2: the reaction of H_2O_2 with KI can produces I_3^- which has an absorption peak at 350 nm, and can be easily determined by UV-vis spectrophotometer (UV-2450, Shimadzu Co., Japan). Thus, a standard curve can be obtained to quantitatively assess the concentration of H_2O_2 in solution. HA-CP@Fe_3O_4 (200 μg mL^{-1}) was dissolved in PBS (pH = 7.4) or NaAc buffer (pH = 5.4) with or without HAase. After various reaction times, the supernatant was magnetically separated, collected, and mixed with KI (0.5 M). Then, the absorbance of I_3^- was measured to determine the amount of H_2O_2. In subsequent experiments with other experimental groups, HAase was added to investigate their activity.

2.4 Determination of catalytic activity

2.4.1 Colorimetric determination of peroxide groups. $KMnO_4$ (50 μg mL^{-1}) was dissolved in an aqueous solution of H_2SO_4 (0.1 M), followed by addition of Fe_3O_4, Fe_3O_4 + H_2O_2, CP@Fe_3O_4, HA-CP@Fe_3O_4, or H_2O_2. The UV-vis spectra of the solutions were measured in the range of 400–650 nm after incubation for 10 min.

2.4.2 Determination of Fenton activity. TMB and MB were used as indicators of $^{\bullet}OH$ to evaluate the Fenton activity of HA-CP@Fe_3O_4. Briefly, HA-CP@Fe_3O_4 (200 μg mL^{-1}) was incubated in NaAc buffer containing HAase (pH = 5.4) for 60 min. Oxidized TMB (oxTMB) was then monitored by monitoring its absorbance at 652 nm by UV-vis spectrophotometer. In addition, the generation of $^{\bullet}OH$ was further verified by determining the absorbance of MB at 665 nm, which can be degraded by $^{\bullet}OH$. HA-CP@Fe_3O_4 (200 μg mL^{-1}) was added to NaAc buffer (pH = 5.4) containing MB (100 μg mL^{-1}), and the absorbance of the supernatant at 665 nm was measured using a UV-vis spectrophotometer every 10 min.

2.4.3 Determination of Russell activity. The solution of DPBF (0.1 mM) in ethanol was added to NaAc buffer containing HA-CP@Fe_3O_4 (200 μg mL^{-1}). The absorbance of the solution at 409 nm was recorded at two-minute intervals using a UV-vis spectrophotometer. Additionally, the electron spin resonance spectroscopy (ESR, EMXPlus-10, Bruker Co., Germany) was used to confirm the ROS generation. The trapping agents

2,2,6,6-tetramethylpiperidine (TEMP) and 5,5-dimethyl-1-pyrrole-*n*-oxide (DMPO) were used to trap $^1O_2$, $^{\bullet}O_2^-$, and $^{\bullet}OH$, respectively. Different ROS were identified at room temperature for HA-CP@Fe_3O_4 (1 mg mL^{-1}) by the captured molecules (100 μL, 100 mM). Subsequently, ROS trapping assays were used to assess the effect of these ROS on antimicrobial activity. Isopropyl alcohol (IPA, 10 mM) was used to capture $^{\bullet}OH$, 1,4-benzoquinone (BQ, 0.1 mM) was used to capture $^{\bullet}O_2^-$, and L-histidine (His, 1 mM) was used to capture $^1O_2$.

2.4.4 GSH scavenging assay. GSH (1 mM) was firstly mixed with HA-CP@Fe_3O_4 (200 μg mL^{-1}). Then, 100 μL of this solution along with DTNB (20 μL, 5 mM) were added to Tris–HCl buffer (pH = 8.5) at appropriate time, followed by incubation for 30 s. UV-vis spectrophotometer was used to measure the absorption spectrum of the solution.

2.5 Determination of antibacterial activity *in vitro*

The plate counting method was employed to assess the *in vitro* antibacterial activity of HA-CP@Fe_3O_4. In brief, *Staphylococcus aureus* (*S. aureus ATCC 12228*) or *Escherichia coli* (*E. coli ATCC 8739*) were cultured in Luria-Bertani (LB) broth and incubated for 12 h at 37 °C in an incubator with a constant temperature. The bacterial suspensions were diluted with PBS (pH = 7.4) to 1×10^8 CFU mL^{-1}. The experiments were divided into a total of six groups as follows: (1) PBS, (2) H_2O_2, (3) Fe_3O_4, (4) Fe_3O_4 + H_2O_2, (5) CP@Fe_3O_4 and (6) HA-CP@Fe_3O_4. The concentrations of the bacterial suspension, material, and H_2O_2 were 1×10^7 CFU mL^{-1}, 30 μg mL^{-1}, and 62.5 μM, respectively. The material solution was mixed with fresh bacterial suspension in a sterile culture tube and co-incubated for 1 h. Following that, 50 μL of the solution was diluted 10^4 times and evenly spread onto the plate. After incubation at 37 °C for 24 hours, the number of colonies on the agar plate was counted and the bacterial viability was determined.

The bacterial morphology was subsequently characterized using a field-emission scanning electron microscope (FE-SEM, GeminiSEM 500, Zeiss, Germany). Following the antimicrobial tests, the bacteria were centrifuged, fixed with 2.5% glutaraldehyde solution overnight, washed with PBS, and then dehydrated in ethanol of varying concentrations (30, 50, 70, 90 and 100%) for 10 min. Finally, 10 μL drops of dehydrated bacterial samples were placed on silica plate, and then analyzed by a field-emission scanning electron microscope (FE-SEM, GeminiSEM 500, Zeiss, Germany).

2.6 Determination of antibacterial activity *in vivo*

Female Balb/c mice (6–8 weeks, Animal Center of Xi'an Jiaotong University) were used for the evaluation of *in vivo* bacteriostatic activity. The hairs from the back of each mice were shaved and the skin was sterilized with 75% ethanol. The mice were anesthetized with isoflurane before creating a circular wound (9 mm diameter) on their back using sterile scissors. A wound model of *S. aureus* infection was established by placing 50 μL of 1×10^8 CFU mL^{-1} *S. aureus* suspension onto the wound and incubating it for 24 h. The mice were randomly divided into six groups (n = 4) as follows: control: Fe_3O_4, Fe_3O_4 + H_2O_2, CP@Fe_3O_4, HA-CP@Fe_3O_4, and HA-CP@Fe_3O_4 + magnetic(M) groups. All these groups received treatment every 24 h using 100 μL (30 μg mL^{-1}) of material solution. Photographs of the three groups of wounds were captured on days 0, 1, 3, 5, and 7, respectively. In addition, the weight of each mouse was regularly monitored using an electronic balance. To evaluate the bacteriostatic effect of different treatments, all mice were euthanized after 7 days of treatment. The wound tissue was collected, and the viable bacteria at the infected site were determined by plate counting method. In addition, the mice were dissected and their wound tissue was soaked in 4% paraformaldehyde aqueous solution. Hematoxylin and eosin (H&E) and Masson reagent were employed to observe the inflammatory response and tissue regeneration of the infected wound. To assess the biosafety of HA-CP@Fe_3O_4, H&E staining was performed on major organs (*i.e.*, heart, liver, spleen, lungs, and kidneys) of mice treated with and without HA-CP@Fe_3O_4. All experimental protocols were approved by the Ethics Committee of Xi'an Jiaotong University Health Science Center (Xi'an, China).

2.7 Cytotoxicity and hemolysis assays

The *in vitro* cytotoxicity of various doses of HA-CP@Fe_3O_4 (0, 12.5, 25, 50, 100, and 200 μg mL^{-1}) on L929 cells was investigated by 3-(4,5-dimethylthiazol-2-yl)-2,5-diphenyl tetrazolium bromide (MTT) test. Briefly, L929 cells were incubated in 96-well plates at 37 °C for 24 h. Then, the nanomaterials were added and incubated for another 24 h. Subsequently, the cells were washed three times with sterile PBS, and 50 μL of MTT solution (5 mg mL^{-1}) was added to each well. The supernatant was taken out after 4 h of incubation at 37 °C, and 100 μL of DMSO was added to each well. The absorbance at 470 nm was measured using a microplate reader.

Hemolysis assay was used to determine the blood compatibility HA-CP@Fe_3O_4. After washing the mice erythrocytes using PBS, the collected erythrocytes (0.4 mL) were suspended in PBS (19.6 mL) to ensure even dispersion. Subsequently, 1 mL of the aforementioned erythrocyte suspension was mixed with varying amounts of HA-CP@Fe_3O_4 (1 mL), and the resulting mixture was incubated for 1 h. The hemolysis rate was determined by measuring the absorbance of the supernatant solution (540 nm). Water-treated and PBS-treated groups were used as controls.

2.8 Statistical analysis

All data were expressed in the form of mean ± standard deviation. Statistical analyses were performed by software SPSS *via* one-way analysis of variance (one-way ANOVA). Significant differences were considered as $^*P < 0.05$, $^{**}P < 0.01$, and $^{***}P < 0.001$.

3. Results and discussion

3.1 Preparation and characterization of HA-CP@Fe_3O_4

The synthetic route of HA-CP@Fe_3O_4 is presented schematically in Fig. 1(a). Firstly, Fe_3O_4–COOH nanoparticles were

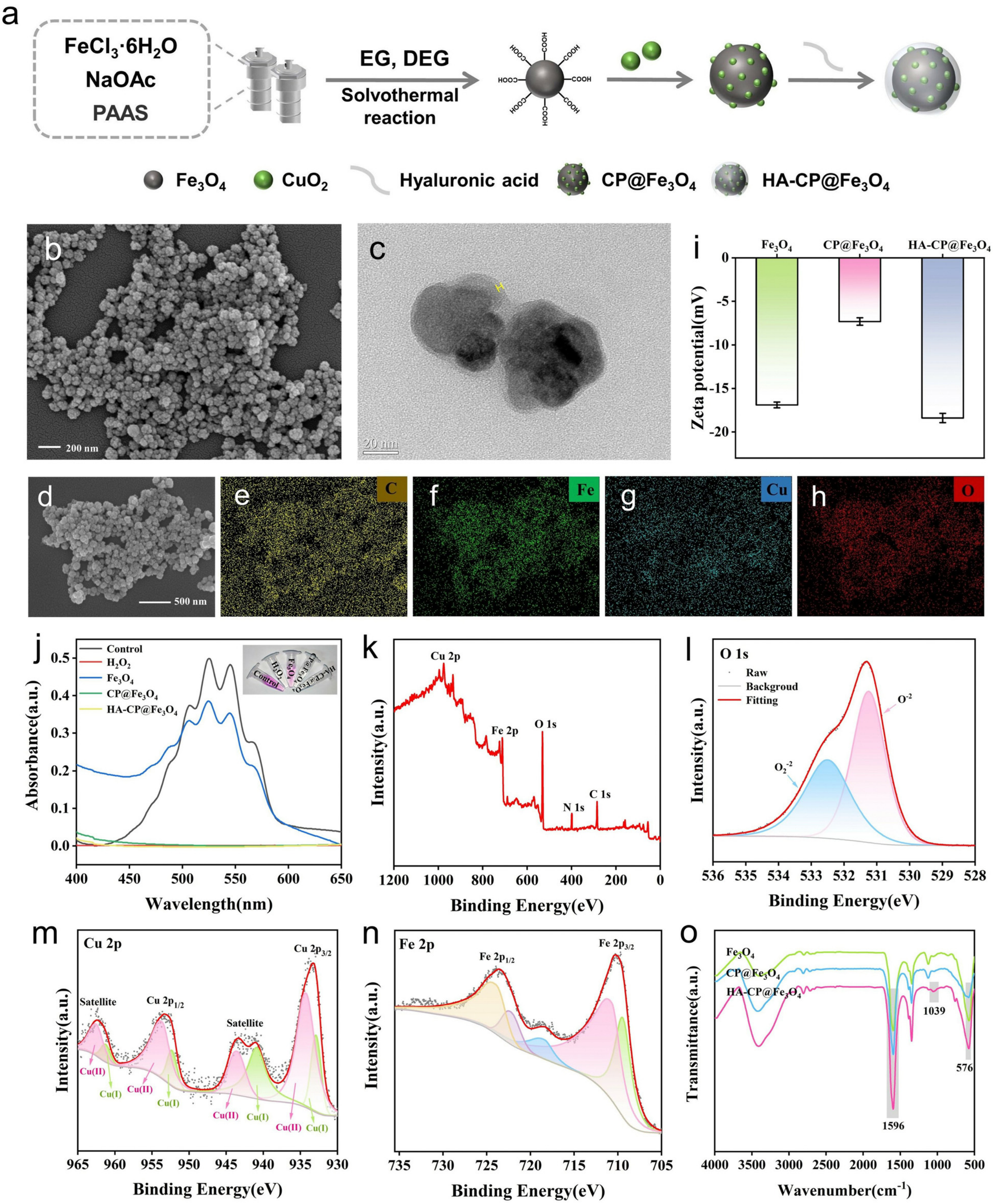

Fig. 1 (a) Schematic illustration of the synthetic route of HA-CP@Fe_3O_4. (b) SEM and (c) TEM images of HA-CP@Fe_3O_4. The yellow lines indicate the thickness of the layers. (d)–(h) EDS elemental mapping images of HA-CP@Fe_3O_4. (i) Zeta potential of Fe_3O_4, CP@Fe_3O_4 and HA-CP@Fe_3O_4. (j) Colorimetric determination of peroxy groups in HA-CP@Fe_3O_4. (k)–(n) XPS spectra of HA-CP@Fe_3O_4. Comparing (o) FTIR spectra of Fe_3O_4, CP@Fe_3O_4 and HA-CP@Fe_3O_4.

synthesized by a simple one-step solvothermal reaction. Then, CuO_2 was generated *in situ* onto their surface to acquire CP@Fe_3O_4. Finally, the nanocomposite HA-CP@Fe_3O_4 was obtained after modification of CP@Fe_3O_4 with HA. Scanning electron microscopy (SEM) reveals that HA-CP@Fe_3O_4 nanoparticles exhibit a coarse spherical morphology with an average particle size of 80 nm (Fig. 1(b)). According to the dynamic light scattering (DLS) analysis, the size of hydrated HA-CP@Fe_3O_4 was found as 102.03 ± 0.99 nm (Fig. S1, ESI†). The presence of distinct layer on the surface of HA-CP@Fe_3O_4 was confirmed by the transmission electron microscopy (TEM), the thickness of which is about 2 nm. (Fig. 1(c)). On the other hand, the element mapping shows the uniform distribution of C, Fe, Cu, and O in HA-CP@Fe_3O_4 (Fig. 1(d)–(h) and Fig. S2, ESI†), asserting the effective loading of CuO_2. The presence of peroxy groups was further verified by $KMnO_4$ colorimetric analysis as shown in the Fig. 1(j). After the introduction of HA-CP@Fe_3O_4, permanganate (MnO_4^-) loses its color under acidic conditions due to the reduction of MnO_4^- to Mn^{2+} by peroxy groups. In addition, the change in zeta potential observed during the preparation process further affirms the successful modification of CuO_2 and HA onto Fe_3O_4 (Fig. 1(i)). Following modification with CuO_2, the zeta potential of Fe_3O_4 shifted from −16.9 to −7.33 mV, and further changed to −18.4 mV upon loading with negatively charged HA.

The chemical structures and detailed composition of nanomaterials were further analyzed by X-ray photoelectron spectroscopy (XPS), X-ray diffraction (XRD), Fourier transform infrared spectroscopy (FTIR), and vibrating sample magnetometer (VSM). XPS was employed to analyze the elements and their valence states in HA-CP@Fe_3O_4. As shown in Fig. 1(k), HA-CP@Fe_3O_4 was mainly composed of C, Fe, Cu, and O elements. An apparent N 1s peak was observed, further demonstrating the existence of the poly(vinylpyrrolidone) (PVP) coating. The presence of two O 1s peaks at 531.3 and 532.5 eV (Fig. 1(l)) can be ascribed to C═O and O–O bonds, respectively, confirming the existence of PVP and peroxo groups in the HA-CP@Fe_3O_4 sample. In addition, the Cu 2p XPS spectrum exhibited two main peaks at 953.64 and 934.26 eV and two satellite peaks at 962.53 and 943.56 eV, indicating that a main valence state of Cu in CuO_2 nanodots was positive bivalence. Meanwhile, the Cu 2p spectrum had two main peaks at 932.9 and 952.32 eV accompanied by two satellite peaks at 940.9 and 961.26 eV, suggesting a certain proportion of Cu^+ possibly due to the decomposition and/or self-reduction of CuO_2 nanodots during synthesis and storage processes. In addition, the ratio of Cu^+/Cu^{2+} was 29.9/71.7, indicating that the principal valence state of Cu in HA-CP@Fe_3O_4 is positive bivalence. The XPS spectrum of Fe 2p (Fig. 1(n)) displays two peaks at 710.9 and 724.6 eV, corresponding to the Fe $2p_{3/2}$ and Fe $2p_{1/2}$ states, respectively. Besides, the Fe 2p peak further splits into two distinct peaks at 709.4 (Fe(II)) and 711.3 eV (Fe(III)). The proportions of Fe(II) and Fe(III) in the HA-CP@Fe_3O_4 were determined as 36% and 64%, respectively based on the inverse fold product of the Fe($2p_{3/2}$) envelope and peak area. Thus, XPS characterization data confirmed the successful preparation of HA-CP@Fe_3O_4. In addition, prepared HA-CP@Fe_3O_4 had a high saturation magnetization (69.14 emu g^{-1}; Fig. S3, ESI†), indicating that HA-CP@Fe_3O_4 has good magnetic properties.

The X-ray diffraction pattern of the prepared samples reveals clear diffraction peaks at 30.26°, 35.54°, 43.24°, 57.12° and 62.76° which corresponds to Fe_3O_4 and are in agreement with the standard cubic spinel Fe_3O_4 phase (JCPDS card 99-0073). (Fig. S4, ESI†) However, no noticeable diffraction peak of CuO_2 was observed in the XRD patterns of CP@Fe_3O_4 and HA-CP@Fe_3O_4. This can be attributed to several factors, including the relatively low copper content (6.43 wt%), ultra-small size, and amorphous nature of CuO_2. By using FTIR spectroscopy, it was possible to locate the characteristic peak of Fe–O in Fe_3O_4 at around 576 cm^{-1}. Typical peaks at 1596 cm^{-1} and 3410 cm^{-1} are attributed to tensile and bending vibrations of O–H. (Fig. 1(o)) Additionally, a notable absorption peak at 1039 cm^{-1} was observed exclusively in HA-CP@Fe_3O_4, which corresponds to the C–O–C asymmetric stretching vibration. All these observations confirm the successful modification of HA and provide additional evidence for the successful synthesis of HA-CP@Fe_3O_4.

3.2 Enzyme-responsive release of copper ions and H_2O_2

Flame atomic absorption spectrometer (FAAS) was employed for monitoring the release of copper ions. As indicated in the Fig. 2(a), significant amount of copper ions were released from HA-CP@Fe_3O_4 when HAase was present in NaAc buffer

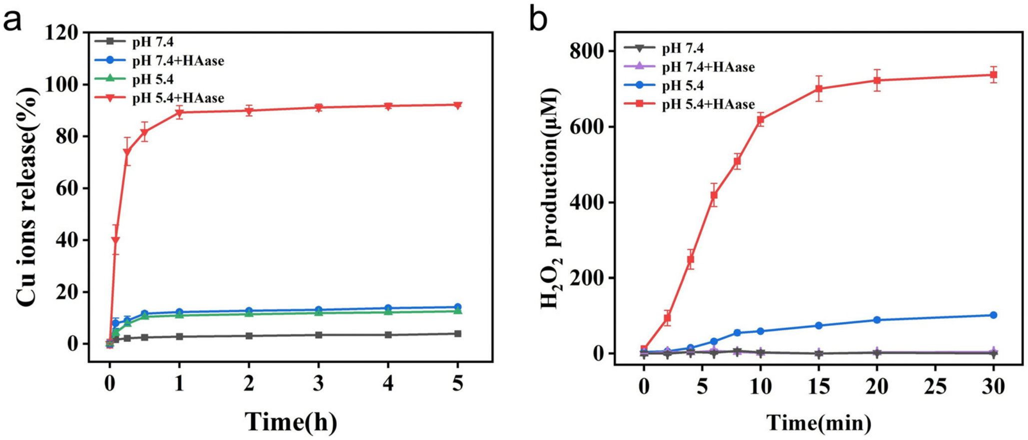

Fig. 2 The release of (a) Cu^{2+} ions and (b) H_2O_2 from HA-CP@Fe_3O_4 under different conditions.

(pH = 5.4), and the equilibrium was achieved in about 1 h. In contrast, when HAase was absent, only 13.4% of copper ions were released which can be attributed to the protection of copper ions by HA. These observations illustrate the enzyme-responsive nature of copper ion release within HA-CP@Fe_3O_4 system. To confirm the absence of copper ion leakage in a neutral environment, the release of copper ions was also examined in PBS (pH = 7.4). As anticipated, the release of copper ions could reach about 15.8% in the presence of HAase, whereas the release of copper ions in the absence of HAase was negligible. Thus, the coating of HA not only prevents copper ions from producing toxic side effects on normal tissues, but also ensures its precise and controlled release at the weakly acidic infection site. These results support the enzyme-responsive behavior of copper ion release in the HA-CP@Fe_3O_4 system.

Under acidic conditions, CuO_2 can undergo decomposition into Cu^{2+} and H_2O_2, and the amount of H_2O_2 released is directly correlated with the amount of ROS generated. In this study, KI was utilized as a probe to detect and quantify H_2O_2 released by HA-CP@Fe_3O_4 under various conditions (Fig. S5, ESI†). The reaction between KI and H_2O_2 leads to the formation of I_3^-, which exhibit a characteristic absorption peak at 350 nm. As depicted in Fig. 2(b), HA-CP@Fe_3O_4 produced up to 738 mol L^{-1} of H_2O_2 when incubated with HAase in NaAc buffer (pH = 5.4), whereas only minimal amounts of H_2O_2 was formed in the absence of HAase. On the other hand, the production of H_2O_2 was negligible in PBS (pH = 7.4). These findings confirm (1) the capability of material to produce H_2O_2 autonomously as well as (2) its ability to trigger H_2O_2 release in response to specific enzymatic activity. Thus, HA-CP@Fe_3O_4 with both autonomous H_2O_2 production and enzyme-responsive H_2O_2 release properties could be a potential nanoagent for precise and augmented CDT.

3.3 Catalytic activity of HA-CP@Fe_3O_4

The ability of synthesized materials (Fe_3O_4, CP@Fe_3O_4 and HA-CP@Fe_3O_4) to generate $^\bullet$OH radicals was investigated using a commonly used probe 3,3′,5,5′-tetramethylbenzidine (TMB). After the oxidation process, the colorless TMB was transformed into blue oxidized TMB (oxTMB). The results indicate that Fe_3O_4 can oxidize the TMB indicator in the presence of H_2O_2 (Fig. 3(a)). Additionally, both CP@Fe_3O_4 and HA-CP@Fe_3O_4 were able to catalyze the oxidation of TMB to blue oxTMB with a distinctive absorption peak at 650 nm in the absence of H_2O_2, demonstrating the superior catalytic activity of materials. The degradation of methylene blue (MB) by various experimental groups was also studied as shown in Fig. 3(f). These results aligned with the findings from TMB experiments, providing further evidence of the efficient production of $^\bullet$OH radicals. Furthermore, a positive correlation between time and MB degradation by HA-CP@Fe_3O_4 was observed (Fig. S6, ESI†). In addition, the TMB method was used to investigate the formation of $^\bullet$OH radicals at various time intervals using different concentrations of HA-CP@Fe_3O_4 to gain deep insights into the catalytic performance of HA-CP@Fe_3O_4. The catalytic activity of HA-CP@Fe_3O_4 was found dependent on both concentration and time (Fig. 3(b) and (c)) and the optimum activity was observed at pH 5.4, which was attributed to the fact that H_2O_2 is generated when CuO_2 decomposes upon acidic conditions. (Fig. S7, ESI†).

Cu(II) has the ability to generate cytotoxic singlet oxygen ($^1O_2$) *via* the Russell reaction. According to the Russell reaction mechanism (Fig. S8, ESI†), the carboxyl group present on the material is initially oxidized by H_2O_2 to form a peroxycarboxylic radical which is then catalytically converted into $^1O_2$ by Cu^{2+}.[44–47] For investigating the Russell catalytic activity of HA-CP@Fe_3O_4, 1,3-diphenylisobenzofuran (DPBF) was used to determine the generation of $^1O_2$. As shown in Fig. 3(d) and (e), the characteristic absorption peaks of CP@Fe_3O_4 and HA-CP@Fe_3O_4-treated DPBF were decreased with time. On contrary, the absorption peaks of Fe_3O_4 and the Fe_3O_4 + H_2O_2 group were nearly same as the blank control group, indicating that CuO_2 was responsible for the generation of $^1O_2$. In addition, the HA-CP@Fe_3O_4-catalyzed generation of $^\bullet$OH and $^1O_2$ was determined by electron spin resonance (ESR) spectroscopy using 5,5-dimethyl-1-pyrrole *n*-oxide (DMPO) and 2,2,6,6-tetramethylpiperidine (TEMP) as the trapping agents. As depicted in Fig. 3(g), the distinctive signals of DMPO–$^\bullet$OH (1 : 2 : 2 : 1) and TEMP–$^1O_2$ (1 : 1 : 1) confirm the production of $^\bullet$OH and 1O2, respectively, while the six-line signal of superoxide anion was invisible. These observations firmly confirms the catalytic ability of HA-CP@Fe_3O_4 to generate $^\bullet$OH and $^1O_2$. Furthermore, the result of ESR assay was verified by scavenging experiments, and the relative oxidation rate (%) decreased by 73.4 and 58.8% after treatment with isopropanol (IPA) and L-histidine (His), respectively. However, the relative oxidation rate was dropped by only 17.1% on addition of $^\bullet O^{2-}$ scavengers, indicating that $^\bullet$OH and $^1O_2$ are the major ROS species produced by HA-CP@Fe_3O_4 (Fig. 3(h)).

An essential intracellular regulatory molecule called glutathione (GSH) exhibits antioxidant properties and aids in maintaining the proper functioning of the immune system. Nevertheless, excessive glutathione produced by bacteria by anaerobic glycolysis in the diseased microenvironment inevitably scavenges ROS and limit antimicrobial actions. Hence, GSH depletion capacity of HA-CP@Fe_3O_4 was assessed by Ellman's reagent assay. In this assay, 5,5′-dithio-bis (2-nitrobenzoic acid) (DTNB) is usually react with the sulfhydryl group of GSH to generate yellow colored 5-thio-2-nitrobenzoic acid, with a maximum absorption peak at 412 nm. Hence, the consumption of HA-CP@Fe_3O_4 for GSH was determined by monitoring the absorbance at 412 nm. As shown in Fig. 3(i), the absorption peak at 412 nm gradually decreased, and the yellow color became lighter as the reaction time increased. This indicates that the residual amount of GSH gradually decreased after treatment with HA-CP@Fe_3O_4, whereas the absorption peak in the control group remained almost unchanged. The outcomes of this experiment proved that HA-CP@Fe_3O_4 exhibits a strong GSH scavenging capability.

3.4 *In vitro* antibacterial activity of HA-CP@Fe_3O_4

Gram-negative *E. coli*, which does not produce HAase, was chosen as the control strain, while Gram-positive *S. aureus*,

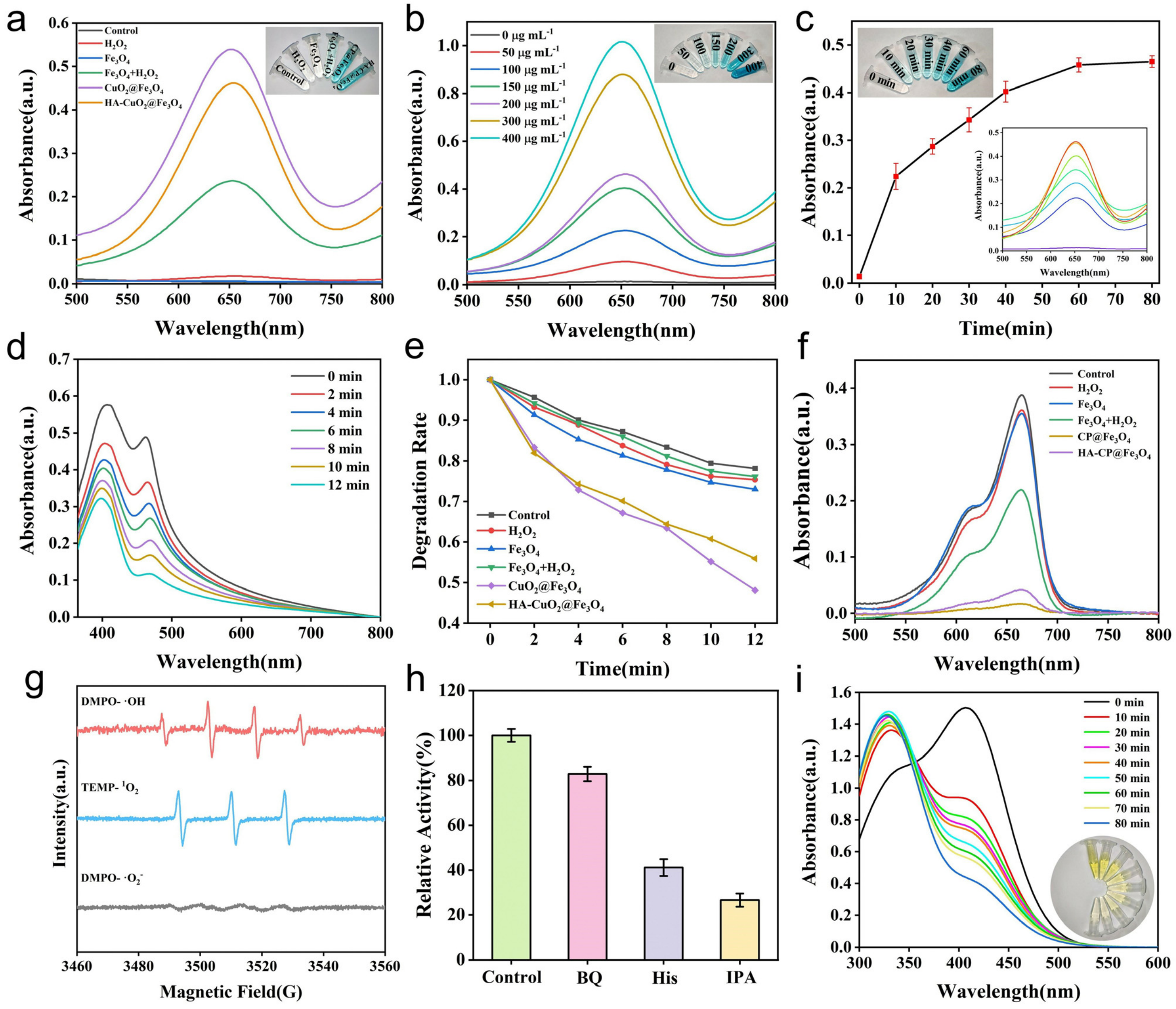

Fig. 3 (a) Confirmation of $^{\bullet}OH$ radicals generated by Fenton-like reaction in different groups (200 μg mL^{-1}) using TMB assay. Studying Fenton activity of HA-CP@Fe_3O_4 by varying (b) concentrations and (c) time (200 μg mL^{-1}). (d) Absorption spectra of DPBF solution with HA-CP@Fe_3O_4 (200 μg mL^{-1}) at increasing time intervals. (e) Comparison of the degradation rates of DPBF over time in different experimental groups (200 μg mL^{-1}). (f) Absorption spectra of MB after treatment with different experimental groups (200 μg mL^{-1}). (g) ESR spin-trapping spectra of HA-CP@Fe_3O_4 for the detection of DMPO–$^{\bullet}OH$, DMPO–$^{\bullet}O_2^-$, and TEMP–$^1O_2$. (h) Inhibition of TMB oxidation by IPA, BQ, and His in the presence of HA-CP@Fe_3O_4. (i) Time-dependent depletion of GSH by HA-CP@Fe_3O_4 (200 μg mL^{-1}).

which does produce HAase, was selected as the model strain to investigate the antimicrobial properties of various nanomaterials (Fe_3O_4, CP@Fe_3O_4 and HA-CP@Fe_3O_4). *S. aureus* and *E. coli* were separately incubated with various nanomaterials, and the bacterial survival rate was subsequently assessed using the plate counting method. As shown in Fig. 4(a)–(c), the results of the PBS group were similar to those of the bare H_2O_2 group and the Fe_3O_4 group, and neither *S. aureus* nor *E. coli* showed any significant harm. It turns out that the $Fe_3O_4 + H_2O_2$ showed some antibacterial effect which can be attributed to the generation of ROS by Fe_3O_4 *via* the Fenton effect. On the other hand, both the CP@Fe_3O_4 and HA-CP@Fe_3O_4 groups showed considerable antibacterial activity against *S. aureus* at a concentration of just 30 μg mL^{-1}, even without the use of H_2O_2. Notably, the HA-CP@Fe_3O_4 group demonstrated superior antibacterial properties compared to CP@Fe_3O_4. As anticipated, the inhibitory effect on *E. coli* (which cannot release HAase) was significantly lower in the HA-CP@Fe_3O_4 group compared to the CP@Fe_3O_4 group, further confirming enzyme-responsive precise antibacterial property of HA-CP@Fe_3O_4. Additionally, it was found that HA-CP@Fe_3O_4 achieved a high bactericidal rate at a very low concentration (30 μg mL^{-1}) without the need for external stimuli (light or heat) and could achieve specific killing of group streptococcus, which is superior to other comparable studies (Table 1). This is due to the fact that the HA coating prevents the decomposition of CuO_2 and minimizes wastage in non-infected areas, enabling precise sterilization while shielding healthy tissues from ROS.

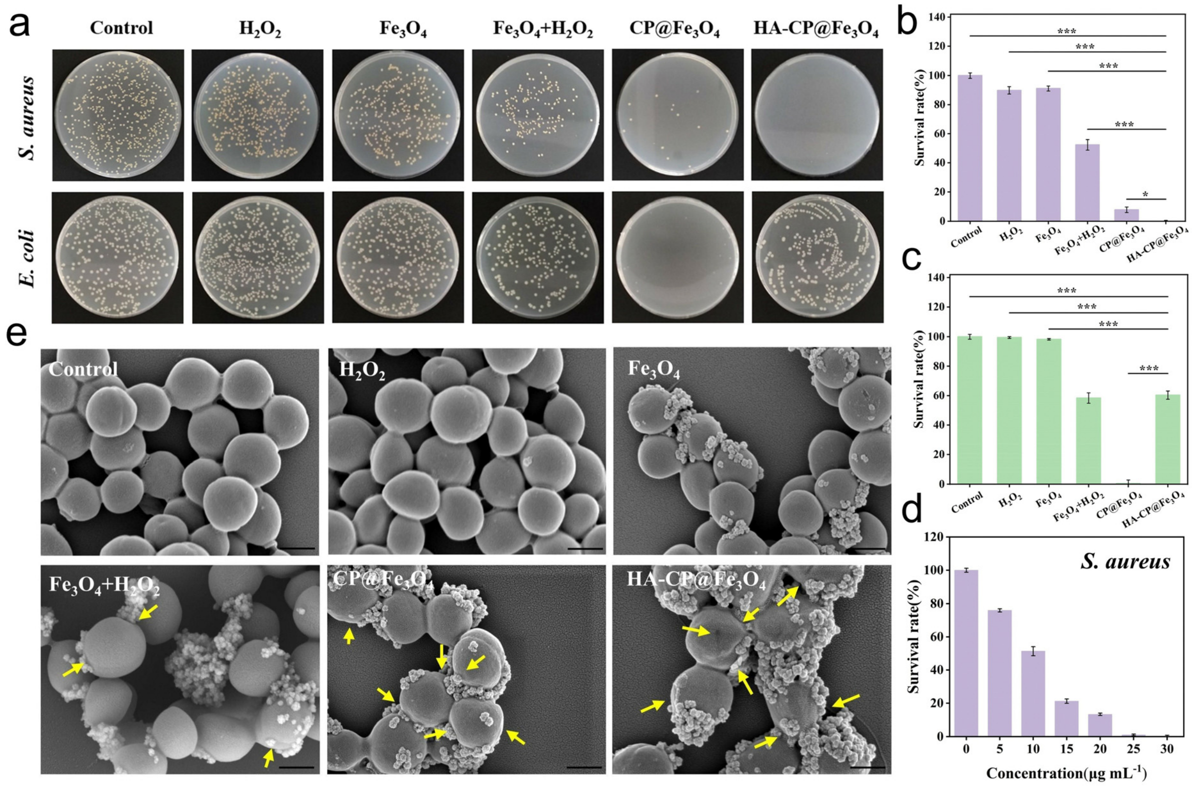

Fig. 4 Study on antibacterial activity of HA-CP@Fe_3O_4 *in vitro*. (a) Images of the LB agar plates of *S. aureus* and *E. coli* after treatment with different experimental groups. (materials concentration: 30 μg mL^{-1}, H_2O_2 concentration 62.5 μM) survival rate of (b) *S. aureus* and (c) *E. coli* after incubation with different groups. (d) Concentration dependent antibacterial activity of HA-CP@Fe_3O_4 against *S. aureus*. (e) SEM images of *S. aureus* after treatment with different experimental groups. Scale bars: 500 nm.

Table 1 Antibacterial model and activity of CuO_2 composite nanomaterials against *S. aureus* at different concentrations

Materials	Antibacterial model	Antibacterial activity (%)	Concentration (μg mL^{-1})	Specificity	Ref.
PDA/CP/ICG	CDT/PDT[a]/PTT[b]	99.9	50	No	27
MoS_2/CuO_2	CDT/PTT	99	50	No	26
CP@WS_2	CDT/PTT	96.56	100	No	48
rGO/CuO_2	PTT/TOT[c]	99	100	No	49
CuO_2@TiO_2	SCDT[d]/STT[e]	99.9	30	No	25
CuO_2@SiO_2	CDT	95	100	No	50
CuO_2	CDT	97.4	37.5	No	51
HA-CP@Fe_3O_4	CDT	99.9	30	Streptococcus	This work

[a] PDT: photodynamic therapy. [b] PTT: photothermal therapy. [c] TOT: topical oxygen therapy. [d] SCDT: sono-chemodynamic therapy. [e] STT: sonothermal therapy.

The antibacterial activity of CP@Fe_3O_4/HA-CP@Fe_3O_4 against *S. aureus* exhibited a concentration-dependent trend, with an increase in concentration resulting in a steady reduction in the bacterial survival rate. (Fig. 4(d) and Fig. S9a–S11a, ESI†). The death rate of *S. aureus* induced by CP@Fe_3O_4/HA-CP@Fe_3O_4 was close to 99.9% at a concentration of 40/30 μg mL^{-1}. In case of *E. coli*, it was necessary to increase the concentration of CP@Fe_3O_4 to 100 μg mL^{-1} to achieve a similar bactericidal rate (Fig. S9b and S11c, ESI†), which was attributed to the robust outer membrane structure of Gram-negative bacteria. However, the antibacterial effect of HA-CP@Fe_3O_4 against *E. coli* did not show a concentration dependence, and when the concentration reached 200 μg mL^{-1}, the antibacterial effect was only 56.3%. It is evident from these results that HA-CP@Fe_3O_4, which incorporates hyaluronic acid as an end-sealing material, can efficiently and selectively kill *S. aureus* and possibly other hyaluronidase-secreting bacteria. Hence, HA-CP@Fe_3O_4 could be a promising chemodynamic antibacterial material for the treatment of infections particularly associated with hyaluronidase secreting bacteria. Although the use of HA sealing material can achieve accurate/selective sterilization, it also has certain disadvantages, such as difficulty in achieving broad spectrum antibacterial effects.

To gain a better understanding of the antimicrobial effect of the materials on *S. aureus*, the morphological alterations of the bacteria after treatment with different materials were investigated using field emission scanning electron microscopy (FE-SEM). As shown in Fig. 4(e), the bacterial morphology remained smooth and free of defects after treatment with H_2O_2 group, Fe_3O_4 group and PBS group alone, exhibiting minimal morphological damage. The presence of minor depression and distortion on the bacterial surface following treatment with Fe_3O_4 + H_2O_2 group indicates some level of damage. In contrast, the bacteria treated with the HA-CP@Fe_3O_4 group and the CP@Fe_3O_4 group exhibited clear signs of cell rupture and collapse (yellow arrows), indicating severe structural damage and injury to the bacteria. The results obtained from both plate antibacterial testing and FE-SEM were largely consistent, providing evidence that the materials possessed excellent and precise *in vitro* antibacterial activity.

3.5 *In vivo* antibacterial activity of HA-CP@Fe_3O_4

Motivated by the remarkable antibacterial action of HA-CP@Fe_3O_4 observed *in vitro*, we investigated the potential of this system for healing and disinfecting animal wounds. The *in vivo* antimicrobial performance of HA-CP@Fe_3O_4 was evaluated by establishing a mouse wound model through injection of *S. aureus* suspension (50 μL, 1 × 10^8 CFU mL^{-1}) into freshly created circular wounds on the back of Balb/c mice, as depicted in Fig. 5(a)–(c). The mice were then randomly divided into six treatment groups as follows: PBS, Fe_3O_4, Fe_3O_4 + H_2O_2, CP@Fe_3O_4, HA-CP@Fe_3O_4, and HA-CP@Fe_3O_4 + M (M refers to magnetic accumulation). The treated wounds have been photographed using a digital camera on a regular basis to assess wound size and healing process in each group as shown in Fig. 5(b). Notably, the HA-CP@Fe_3O_4 + M group showed the best healing outcomes, demonstrating superior effectiveness compared to other groups. To accurately compare the wound healing process among different groups, the relative wound area of each group was quantified (Fig. 5(c) and (e)). After 7 days of treatment, the relative wound areas for the PBS, Fe_3O_4, Fe_3O_4 + H_2O_2, CP@Fe_3O_4, HA-CP@Fe_3O_4, and HA-CP@Fe_3O_4 + M

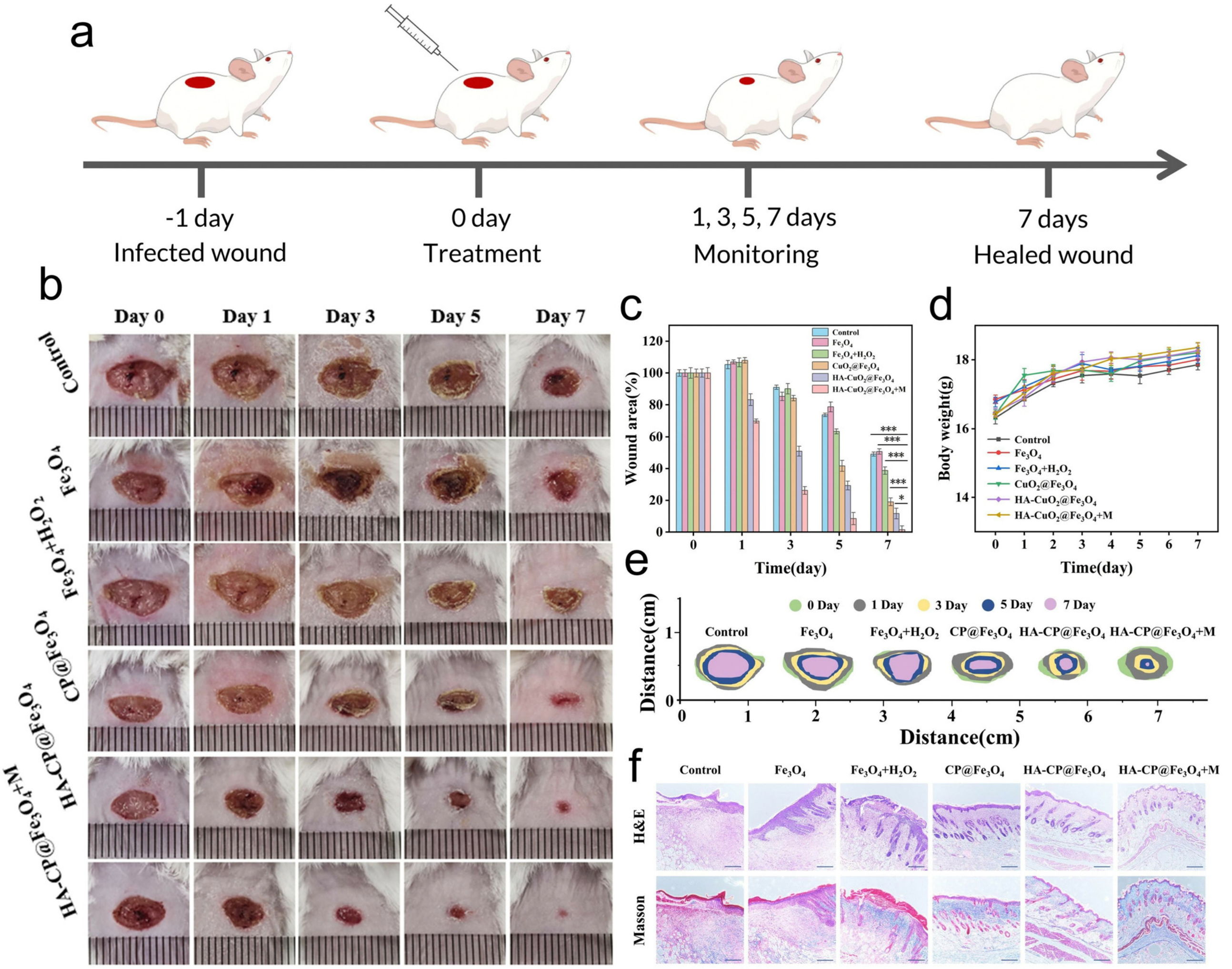

Fig. 5 Study on antibacterial activity of HA-CP@Fe_3O_4 *in vivo*. (a) Schematic of the wound healing process. (b) Representative images of skin wounds after treatment with different groups (30 μg mL^{-1}). (c) Quantitative analysis of wound area for each group at different time points. (d) Change in body weight of mice in different treatment groups during the wound-healing process. (e) Dynamic process diagram illustrating the wound healing progression for each treatment group. (f) H&E staining and Masson staining of wounded tissues. Scale bars: 200 μm.

treatment groups were determined to be 49.2, 50.7, 38.7, 19.1, 11.7, and 1.5%, respectively. As anticipated, the HA-CP@Fe_3O_4 + M treatment group exhibited the most favorable wound healing and scabbing outcomes. The results imply that HA-CP@Fe_3O_4 aggregated at the infection site under the influence of a magnetic field can produce ROS to achieve adequate antimicrobial effects *in vivo*. Importantly, the body weight of mice did not show significantly changes across the different treatments, suggesting that none of the treatment groups impeded the normal growth of mice (Fig. 5(d)).

The wound healing capacity was determined by collecting wound tissues from each group of mice on day 7 following treatment and staining with hematoxylin and eosin (H&E) (Fig. 5(f)). Severe inflammatory cell infiltration was observed in the PBS and Fe_3O_4 group. In contrast, the HA-CP@Fe_3O_4 + M group showed obvious and intact epidermal-dermal connections, along with significant reduction in inflammatory infiltration, suggesting remarkable wound healing capacity of HA-CP@Fe_3O_4. Masson staining was employed to closely examine the growth of collagen fibers in skin tissues. Remarkably, the HA-CP@Fe_3O_4 + M group exhibited the highest concentration of collagen fibers compared to the PBS and Fe_3O_4 groups, which showed the lowest amount of collagen fibers. Additionally, the HA-CP@Fe_3O_4 + M group showed a notable increase in hair follicle regeneration, demonstrating successful tissue regeneration. After 7 days of treatment, the infected tissue was removed for plate counting to conduct further *in vivo* antimicrobial assessment. As depicted in Fig. S12 and S13 (ESI†), the HA-CP@Fe_3O_4 + M group displayed the lowest number of bacterial colonies among all the groups. In conclusion, the HA-CP@Fe_3O_4 nanomaterials exhibit outstanding *in vivo* wound healing and antimicrobial activities.

3.6 Cytotoxicity of HA-CP@Fe_3O_4

Biocompatibility has always been the primary safety criterion for *in vivo* application of antimicrobial nanoplatforms. In order to assess the overall biocompatibility of HA-CP@Fe_3O_4, we conducted assessments of its cytocompatibility and hemocompatibility. By using the MTT assay, the toxicity of HA-CP@Fe_3O_4 for L929 cells was initially evaluated. As depicted in Fig. 6(b), even at a concentration of 200 μg mL^{-1}, more than 85% of the cells remained viable, proving that HA-CP@Fe_3O_4 exhibited minimal cytotoxicity. In addition, we further evaluated the cytocompatibility of CP@Fe_3O_4, the results indicate that the biocompatibility of CP@Fe3O4 is slightly lower than that of HA-CP@Fe_3O_4 (Fig. S14, ESI†). However, at a concentration of 100 μg mL^{-1} (determined as the *in vitro* antibacterial concentration against *E. coli*) of CP@Fe_3O_4, the viability of L929 cells remains above 80%. Therefore, CP@Fe_3O_4 may be utilized for the treatment of certain infections caused by multiple bacterial strains, but there is a potential risk of compromising the biocompatibility of CP@Fe_3O_4.

The hemolytic activity test was conducted to evaluate the potential hemolytic performance of HA-CP@Fe_3O_4 by co-incubating various concentrations of HA-CP@Fe_3O_4 with mouse erythrocytes. The results demonstrated that the supernatants of various concentrations of HA-CP@Fe_3O_4-treated groups resembled those of the negative control (PBS) group in terms

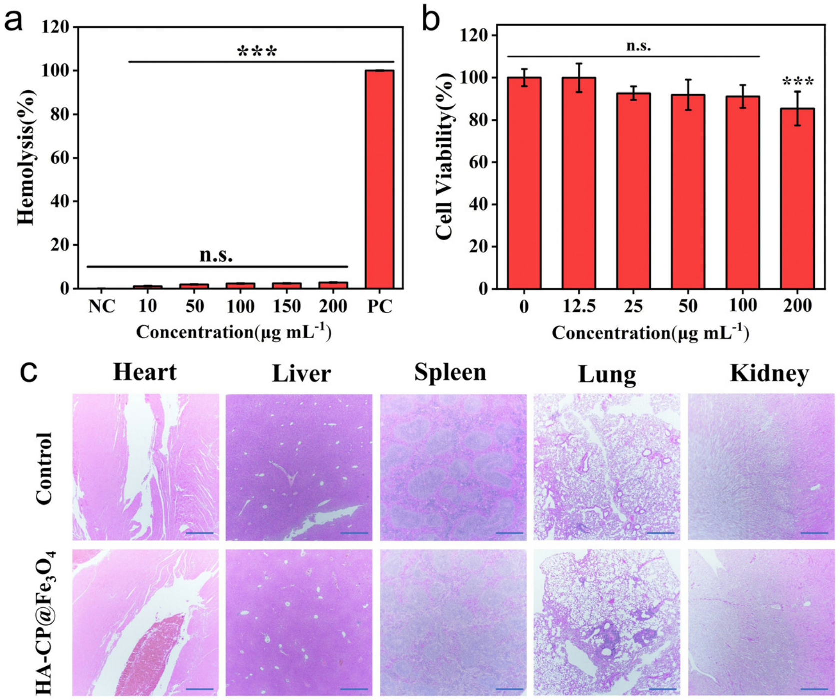

Fig. 6 (a) Hemolysis assay using HA-CP@Fe_3O_4 dispersions at different concentrations. Water is the positive control (PC), and PBS is the negative control (NC). (b) The survival rate of L929 cells after treatment with different concentrations of HA-CP@Fe_3O_4 for 24 h. (c) H&E staining images of the major organs (heart, liver, spleen, lungs, and kidneys) of mice from two different groups after 7 days. Scale bar = 500 μm.

of being translucent and colorless (Fig. 6(a)). Even at a concentration of 200 μg mL^{-1}, the HA-CP@Fe_3O_4 did not cause significant hemolysis of erythrocytes, with a hemolysis rate of only 2.85%. These findings indicate that the material poses excellent blood compatibility and further support its safety for potential biomedical applications. Finally, H&E staining was conducted on vital organs, including the heart, liver, spleen, lungs, and kidneys, to assess the *in vivo* biosafety of HA-CP@Fe_3O_4 (Fig. 6(c)). The lack of any visible histologic abnormalities or organ damage in mice treated with HA-CP@Fe_3O_4 demonstrated that the drug has favorable *in vivo* biosafety.

4. Conclusions

In summary, we have developed an on-demand chemodynamic antimicrobial nanoplatform (HA-CP@Fe_3O_4) with self-supply of H_2O_2 by successfully coating enzyme-responsive HA onto CuO_2-loaded Fe_3O_4 nanoparticles. Under weakly acidic conditions, HA-CP@Fe_3O_4 not only generates $^{\bullet}OH$ radicals to facilitate H_2O_2 self-supplying controlled-release CDT *via* the Fenton effect but also produces $^1O_2$ for synergistic sterilization through the Russell effect, enabling synergistic antimicrobial therapy. Furthermore, the encapsulation of HA provides (1) a targeting affect against HAase-secreting microorganisms, (2) protection against cytotoxicity, and (3) prevents resource waste due to improper copper ion release. Additionally, HA has the beneficial effect of accelerating the wound healing. *In vivo* studies confirm that the magnetic aggregation of HA-CP@Fe_3O_4 on the wound can accelerate the healing process while maintaining the excellent hemocompatibility and cytocompatibility. Overall, this study presents a novel and effective on-demand antimicrobial platform with self-supplied H_2O_2, showing great potential for the clinical treatment of bacteria-infected wounds.

Author contributions

Sijie Zhang: validation, methodology, writing original draft. Sameer Hussain: conceptualization, data curation. Yuhai Tang: conceptualization, supervision. Kaili Wang: validation, data curation. Xingyan Wang: investigation, methodology. Long Zhang: validation. Yuheng Liao: data curation. Chen Wang: data curation. Yi Hao: conceptualization, investigation, data curation. Ruixia Gao: project administration, supervision, funding acquisition. All persons who have made substantial contributions to the work reported in the manuscript.

Conflicts of interest

There are no conflicts to declare.

Acknowledgements

This work was supported by the National Natural Science Foundation of China (no. 22250410261), the Natural Science Foundation of Shaanxi Province (no. 2023-YBNY-233), and the Ministry of Science & Technology, China for foreign youth talent support program (no. QN2021170004L). The authors thank Junjie Zhang (School of Chemistry) and Xiaojing Zhang (School of physics), Xi'an Jiaotong University, for the help with material characterizations.

References

1 P. Sunil, R. Shristi and A. Bipin, *BMJ Global Health*, 2019, **4**, e002104.
2 D. Raoult, M. Leone, Y. Roussel and J.-M. Rolain, *Lancet Infect. Dis.*, 2019, **19**, 128–129.
3 J. H. Kwon and W. G. Powderly, *Science*, 2021, **373**, 471.
4 A. Hassoun, P. K. Linden and B. Friedman, *Crit. Care*, 2017, **21**, 211.
5 D. Alrahmany, L. Pontiggia and I. Ghazi, *Int. J. Infect. Dis.*, 2020, **101**, 158.
6 H. Isenman and D. Fisher, *Curr. Opin. Infect. Dis.*, 2016, **29**, 577–582.
7 E. Scherer, B. Beall and B. Metcalf, *Emerging Infect. Dis.*, 2021, **27**, 1689.
8 B. Kuehn, *JAMA*, 2019, **322**, 2376.
9 S. B. Levy and B. Marshall, *Nat. Med.*, 2004, **10**, S122–S129.
10 Y. Wang, Y. Yang, Y. Shi, H. Song and C. Yu, *Adv. Mater.*, 2020, **32**, 1904106.
11 Y. Chen, Y. Gao, Y. Chen, L. Liu, A. Mo and Q. Peng, *J. Controlled Release*, 2020, **328**, 251–262.
12 A. Anas, J. Sobhanan, K. M. Sulfiya, C. Jasmin, P. K. Sreelakshmi and V. Biju, *J. Photochem. Photobiol., C*, 2021, **49**, 100452.
13 L. Lai, W. Zou, Y. Zhang, Y. Tu, S. Li, T. Xin, T. Zhou, S. Xu, P. Zheng, Q. Pan and W. Zhu, *Chem. Eng. J.*, 2022, **435**, 135084.
14 Q. Wang, J. Jiang and L. Gao, *Wiley Interdiscip. Rev.: Nanomed. Nanobiotechnol.*, 2022, **14**, e1769.
15 Z. Tang, P. Zhao, H. Wang, Y. Liu and W. Bu, *Chem. Rev.*, 2021, **121**, 1981–2019.
16 C. Jia, Y. Guo and F.-G. Wu, *Small*, 2022, **18**, 2103868.
17 F. Gao, X. Li, T. Zhang, A. Ghosal, G. Zhang, H. M. Fan and L. Zhao, *J. Controlled Release*, 2020, **324**, 598–609.
18 X. Li, R. Luo, X. Liang, Q. Wu and C. Gong, *Chin. Chem. Lett.*, 2022, **33**, 2213–2230.
19 Y. Zhang, W. Liu, Y. Huang, Y. Wang, X. Chen and Z. Chen, *Chem. Eng. J.*, 2022, **446**, 137214.
20 Q. Tian, F. Xue, Y. Wang, Y. Cheng, L. An, S. Yang, X. Chen and G. Huang, *Nano Today*, 2021, **39**, 101162.
21 Y. Sang, F. Cao, W. Li, L. Zhang, Y. You, Q. Deng, K. Dong, J. Ren and X. Qu, *J. Am. Chem. Soc.*, 2020, **142**, 5177–5183.
22 L. Feng, R. Xie, C. Wang, S. Gai, F. He, D. Yang, P. Yang and J. Lin, *ACS Nano*, 2018, **12**, 11000–11012.
23 L.-S. Lin, T. Huang, J. Song, X.-Y. Ou, Z. Wang, H. Deng, R. Tian, Y. Liu, J.-F. Wang, Y. Liu, G. Yu, Z. Zhou, S. Wang, G. Niu, H.-H. Yang and X. Chen, *J. Am. Chem. Soc.*, 2019, **141**, 9937–9945.

24 M. Li, X. Lan, X. Han, S. Shi, H. Sun, Y. Kang, J. Dan, J. Sun, W. Zhang and J. Wang, *ACS Appl. Mater. Interfaces*, 2021, **13**, 29269–29280.

25 M. Liang, L. Shang, Y. Yu, Y. Jiang, Q. Bai, J. Ma, D. Yang, N. Sui and Z. Zhu, *Acta Biomater.*, 2023, **158**, 811–826.

26 J. Li, W. Yi, Y. Luo, K. Yang, L. He, C. Xu, L. Deng and D. He, *Acta Biomater.*, 2023, **155**, 588–600.

27 J. Xiao, L. Hai, K. Yang, Y. Luo, Z. Wang, J. Li, C. Ou, L. Wang, L. Deng and D. He, *Chem. Eng. J.*, 2023, **465**, 142958.

28 A. Allafchian, F. Karimzadeh, A. Valikhani and A. Seraj, *Int. J. Biol. Macromol.*, 2023, **251**, 126418.

29 Y. Sun, W. Yue, B. Niu, Y. Lin, X. Liu, T. Wu, G. Zhang, K. Qu, L. Wang and Y. Niu, *J. Mater. Chem. B*, 2023, **11**, 3434–3444.

30 F. Yu, C. Jia, X. Wu, L. Sun, Z. Shi, T. Teng, L. Lin, Z. He, J. Gao, S. Zhang, L. Wang, S. Wang and X. Zhu, *Nat. Commun.*, 2023, **14**, 4975.

31 J. Feng, X. Yang, T. Du, L. Zhang, P. Zhang, J. Zhou, L. Luo, H. Sun, Y. Han, L. Liu, Y. Shen, J. Wang and W. Zhang, *Adv. Sci.*, 2023, **10**, 2303078.

32 T. Du, S. Wang, J. Feng, Y. Shen, J. Wang and W. Zhang, *Nano Lett.*, 2023, **23**, 9563–9570.

33 Y. Zhang, J. Li and P. Habibovic, *Bioact. Mater.*, 2022, **15**, 372–381.

34 Z. Zhang, Y. Fang, L. Zhuo, H. Yuan and L. Zhang, *J. Alloys Compd.*, 2022, **904**, 164001.

35 S. Ma, S. Zhan, Y. Jia and Q. Zhou, *ACS Appl. Mater. Interfaces*, 2015, **7**, 21875–21883.

36 Y. Xu, K. Wang, S. Zhao, Q. Xiong, G. Liu, Y. Li, Q. Fang, X. Gong and S. Xuan, *Chem. Eng. J.*, 2022, **437**, 135282.

37 T. Liu, B. Cai, P. Yuan, L. Wang, R. Tian, T. Dai, L. Weng and X. Chen, *Biomater. Sci.*, 2023, **11**, 2590–2602.

38 Y. Liu, K. Guo, M. Ding, B. Zhang, N. Xiao, Z. Tang, Z. Wang, C. Zhang and Q. T. H. Shubhra, *ACS Appl. Mater. Interfaces*, 2022, **14**, 42541–42557.

39 Y. Liu, Y. Liang, P. Lei, Z. Zhang and Y. Chen, *Adv. Sci.*, 2023, **10**, 2203669.

40 Y. Feng, D. Ding, W. Sun, Y. Qiu, L. Luo, T. Shi, S. Meng, X. Chen and H. Chen, *ACS Appl. Mater. Interfaces*, 2019, **11**, 37461–37470.

41 N. Devnarain, N. Osman, V. O. Fasiku, S. Makhathini, M. Salih, U. H. Ibrahim and T. Govender, *Wiley Interdiscip. Rev.: Nanomed. Nanobiotechnol.*, 2021, **13**, e1664.

42 G. Baier, A. Cavallaro, K. Vasilev, V. Mailänder, A. Musyanovych and K. Landfester, *Biomacromolecules*, 2013, **14**, 1103–1112.

43 M. Mohammed, N. Devnarain, E. Elhassan and T. Govender, *Wiley Interdiscip. Rev.: Nanomed. Nanobiotechnol.*, 2022, **14**, e1799.

44 S. Miyamoto, G. R. Martinez, M. H. G. Medeiros and P. Di Mascio, *J. Am. Chem. Soc.*, 2003, **125**, 6172–6179.

45 S. Miyamoto, G. R. Martinez, M. H. G. Medeiros and P. Di Mascio, *J. Photochem. Photobiol., B*, 2014, **139**, 24–33.

46 G. Liu, J. Zhu, H. Guo, A. Sun, P. Chen, L. Xi, W. Huang, X. Song and X. Dong, *Angew. Chem., Int. Ed.*, 2023, **62**, e202306404.

47 Z. Wang, B. Liu, Q. Sun, S. Dong, Y. Kuang, Y. Dong, F. He, S. Gai and P. Yang, *ACS Appl. Mater. Interfaces*, 2020, **12**, 17254–17267.

48 X. Xie, R. Wang, X. Zhang, Y. Ren, T. Du, Y. Ni, H. Yan, L. Zhang, J. Sun, W. Zhang and J. Wang, *Appl. Catal., B*, 2021, **295**, 120315.

49 M. Jannesari, O. Akhavan, H. R. Madaah Hosseini and B. Bakhshi, *ACS Appl. Mater. Interfaces*, 2020, **12**, 35813–35825.

50 X. Li, M. Liang, S. Jiang, S. Cao, S. Li, Y. Gao, J. Liu, Q. Bai, N. Sui and Z. Zhu, *ACS Appl. Mater. Interfaces*, 2021, **13**, 22169–22181.

51 R. Zhang, G. Jiang, Q. Gao, X. Wang, Y. Wang, X. Xu, W. Yan and H. Shen, *Nanoscale*, 2021, **13**, 15937–15951.